A survey of water production in 61 comets from SOHO/SWAN observations of hydrogen Lyman-alpha: Twenty-one years 1996–2016

Michael Combi, Terhi T. Mäkinen, Jean-Loup Bertaux, Eric Quémerais, Stéphane Ferron

HAL Id: insu-01876371
https://insu.hal.science/insu-01876371

Submitted on 25 Nov 2020

A Survey of Water Production in 61 Comets from SOHO/SWAN Observations of Hydrogen Lyman-alpha: Twenty-One Years 1996-2016

Short Title: Water Production in Comets 1996-2016

M.R. Combi[1], T.T. Mäkinen[2], J.-L. Bertaux[3], E. Quémerais[3],
S. Ferron[4]

[1]Dept. of Climate and Space Sciences and Engineering

University of Michigan

2455 Hayward Street

Ann Arbor, MI 48109-2143

*Corresponding author: mcombi@umich.edu

[2]Finnish Meteorological Institute, Box 503

SF-00101 Helsinki, FINLAND

[3] LATMOS/IPSL

Université de Versailles Saint-Quentin

11, Boulevard d'Alembert, 78280, Guyancourt, FRANCE

[4]ACRI-ST, Sophia-Antipolis, FRANCE

6 Tables

9 Figures

Abstract

The Solar Wind Anisotropies (SWAN) instrument on the SOlar and Heliospheric Observatory (SOHO) satellite has observed 44 long period and new Oort cloud comets and 36 apparitions of 17 short period comets since its launch in December 1995. Water production rates have been determined from the over 3700 images producing a consistent set of activity variations over large parts of each comet's orbit. This has enabled the calculation of exponential power-law variations with heliocentric distance of these comets both before and after perihelion, as well as the absolute values of the water production rates. These various measures of overall water activity including pre- and post-perihelion exponents, absolute water production rates at 1 AU, active surface areas and their variations have been compared with a number of dynamical quantities for each comet including dynamical class, original semi-major axis, nucleus radius (when available), and compositional taxonomic class. Evidence for evolution of cometary nuclei is seen in both long-period and short-period comets.

1. Introduction

The Solar Wind ANisotropies (SWAN) instrument on board the SOlar and Heliospheric Observatory (SOHO) satellite has been operating in a halo orbit around the Earth-Sun L1 Lagrange point since shortly after its launch on 2 December 1995. Its primary science mission has been to provide continuous monitoring of the whole sky distribution of hydrogen Lyman-alpha emission resulting from interplanetary atomic hydrogen streaming through the solar system and being eaten away by charge exchange, electron impact and ionization by the sun and solar wind and being illuminated by the Sun's Ly-α emission. Because of the required sensitivity and the ability to observe the full sky, SWAN has

also been an excellent platform from which to observe the hydrogen Ly-α comae of many comets since the beginning of 1996. After more than 20 years in operation it is still providing excellent measurements of hydrogen in both the interplanetary medium (Bertaux et al., 1995) and comets (Bertaux et al. 1998). SWAN has provided important observations of many individual comets. The SWAN observations allowed to determine that a total of $2.7 \pm 0.4 \ 10^9$ kg of water ice was lost by comet 67P during one perihelion passage in average (Bertaux et al., 2015). Combined with the estimated area of 20 km^2, it yields an equivalent thickness of 15 cm of ice sublimated inside the nucleus and lost to space in one perihelion passage of this comet. SWAN observations also allowed for important coverage of the EPOXI mission target comet 103P/Hartley 2 from previous apparitions (Combi et al. 2011b) and providing coverage throughout the apparition of the flyby (Combi et al. 2011b). Finally, SWAN observations of comet 2012 S1 (ISON) by Combi et al. (2014) allowed for the determination of the water lost by the comet before its total disruption and loss at its very close perihelion passage, which is consistent with pre-perihelion estimates of the size of the nucleus (Lamy et al., 2014).

Most long-term surveys of cometary activity concentrate on composition (Newburn and Spinrad, 1989; A'Hearn et al. 1995; Fink and Hicks 1996; Fink 2009; Langland-Shula and Smith 2011; Cochran et al. 2012; Dello Russo et al. 2016), although A'Hearn et al. (1995) did examine heliocentric distance dependencies of water proxies like OH or even CN. The Nançay radio survey of 18-cm lines of OH in comets (Crovisier et al. 2002), on the other hand, covers OH observations and thus mainly water production rates. Similarly, this survey covers the water production rates of 61 comets each observed over extended periods of time allowing for exponential power-law exponents and production rates at 1 AU to be computed for pre- and post-perihelion legs of the comet orbits. Most of the long period comets included in this survey were observed after most of the comets included most of the published surveys so detailed comparisons with compositional taxonomic classes do not include many overlapping comets. One exception is the recent infrared survey of Dello Russo et al. (2016), however

their IR taxonomy is rather involved providing depleted, typical and enhanced classification for 10 different molecular species compared to H_2O. Unfortunately even for the IR survey there are not enough common comets to make meaningful cross-comparisons. However, Dello Russo et al. looked at the literature for the visual observations of the common carbon radicals and list those taxonomic classes (depleted or typical) for several comets in the SWAN dataset.

2. Observations and Basic Model Analysis

The SWAN all-sky camera consists of two systems one for the north heliographic hemisphere and the other for the south. Each has a 5x5 array of detectors of one square degree each that are scanned across the sky every day yielding a full sky map of hydrogen Ly-α emission. Depending on location in the sky with respect to the Sun and the galactic equator, comets brighter than magnitude ~10-12 can be detected by SWAN. During the first 10 years of operation, SWAN was at times targeted specifically at comets with increased exposure time and spatial double-oversampling the one square degree pixels. The detector is actually a broadband far ultraviolet detector, which has sensitivity to either side of Lyα, however for comets, nearly 98% of the total far ultraviolet emission is typically in Lyα, and all the other emissions, e.g., O, C, S, CO, etc., are concentrated well within the innermost 1-degree pixel centered on the nucleus. For our analyses we normally sample the coma out to a radius of 8 degrees. The extra total non-Lyα signal is quite small and accounted for in our stated uncertainties. While comets are observed at quite a range of geocentric distance within this 8 degree radius aperture, this distance is nearly always larger than the effective production scale length of H atoms resulting from photodissociation of H_2O and OH and nearly always smaller than the decay scale length of the outward streaming fast H atoms. Therefore, there should be no systematic error resulting from the sampling size of the production rate calculation. Such effects as they relate to typical photometric and spectrophotometric observations of the common visible radicals (C_2, C_3, CN, NH_2, NH and OH), were

on the other hand shown to be quite sensitive to the choice of model parameters (Fink and Combi, 2004) and could yield systematic differences in determined abundances and production rates.

Over 90% of observed hydrogen atoms in comets are produced by the photodissociation of H_2O molecules and the subsequent photodissociation of OH with typically 6%±3% coming from all other sources (Combi et al., 2005). Nascent H atoms are produced with a range of speeds of 8 - 20 km s^{-1} resulting from the excess energy of photodissociation (Keller and Meier, 1976; Combi et al., 2004). The combination of photodissociation rate and water production rate, both of which increase as a comet's heliocentric distance decreases, determine the fraction of H atoms that collide with the heavy molecules, mostly water, in the inner coma. When this happens in sufficient numbers the transfer of energy results in the slowing of H atoms and heating of the heavy molecules, which results in a faster expanding coma. The shaping of the H atom speed distribution and the resulting physical effect on the expansion of the coma have been observed and quantified quite well (Bockelée-Morvan & Crovisier, 1987; Combi & Smyth, 1988a&b; Combi, 1989; Combi et al., 1998; Combi et al., 2000; Tseng et al., 2007; Shou et al., 2016).

SWAN images of the H Lyα coma are analyzed with a method called the time-resolved model (TRM) that was described in the paper by Mäkinen & Combi (2005) and combines aspects of several past modeling approaches, namely, the vectorial model (Festou, 1981); the syndyne model (Keller and Meier, 1976), and the particle kinetic physics models (Combi & Smyth 1988a&b). Input parameters to the model include the comet's orbital elements obtained from the JPL Horizons web site (http://ssd.jpl.nasa.gov/horizons.cgi), the SOHO orbit obtained from the SOHO project, and the daily solar Lyα flux at the Earth obtained from the LISRD web site at LASP, University of Colorado, (http://lasp.colorado.edu/lisird/lya/). The solar Lyα flux at the comet is estimated by taking the nearest value at the Earth facing the same part of the Sun correcting for the difference in heliographic longitude between the Earth and the comet. The fraction of H atoms thermalized by collisions with the water

dominated coma and the resulting velocity distribution of H atoms leaving the inner coma is calculated from a parameterized version of the hybrid fluid/kinetic model calculations (Combi & Smyth, 1988a&b; Combi et al., 2000).

As an example Figure 1 shows the portion of the full-sky image of 1 November 2011 centered on comet C/2009 P1 (Garradd) from the results of Combi et al. (2013) that is part of the TRM analysis. The aperture for summing up the comet Lyα emission is an 8-degree radius circle centered on the comet, shown in gray. The outer region of the IPM background with field stars is shown in blue. The red areas are the locations of field stars that are masked off so as not to count those in the comet brightness for optimizing the model fit. The TRM fits a comet distribution as described above and a tilted background for the IPM in first or second order. Figure 2 shows the profile of brightness that corresponds to the cut shown as the red line in Figure 1. The observed comet profile is in white, the modeled comet profile in green and the subtracted IPM line shown as the darker straighter green line below. The masked star contribution is shown in red and regions outside the comet as part of the IPM are shown in blue. The result of each TRM model analysis is to produce a water production from each image.

In addition to calculating the average water production rate for each image the TRM, as described by Mäkinen and Combi (2005) also employs a method to analyze long sequences of images together to deconvolve the daily water production rates at the nucleus. When comets are bright enough this method can be used to track secular variations of the initial water production rate at the nucleus rather than just the average value responsible for the hydrogen distribution within several degrees of the nucleus. Results of this procedure have been published for a number of comets in the past, namely comet C/1996 B2 (Hyakutake) by Combi et al. (2005), comets 1999 H1 (Lee), 1999 T1 (McNaught-Hartley), C/2001 A2 (LINEAR), C/2000 WM1 (LINEAR) and 153P/Ikeya-Zhang by Combi et al. (2008) and C/2012 S1 (ISON) by Combi et al. (2014). In such cases we can compare with other

6

observations taken of shorter-lived species and closer to the nucleus and compare shorter-term temporal variations such as outbursts. Making such comparisons shows that the normal single image production rates delays and averages the water production rate over a time period of about 1 to 3 days depending on the distance to the comet. Therefore, an abrupt outburst is both delayed and smoothed out over up to 3 days as seen in the response of a single hydrogen coma image. None of the results given in this survey depend on the deconvolution processing.

The remainder of this paper describes summary results of 44 new/long-period comets and 39 apparitions of 17 short period comets observed by SOHO/SWAN since 1996 and analyzed with the TRM. Most of the data have already been archived and certified in the Small Bodies Node (SBN) of the NASA Planetary Data System (PDS), which can be found at Combi (2017). The results of 9 newer long-period comets observed since 2012 have been recently published by Combi et al. (2018) and will be submitted to the PDS in 2018. Results of the most recent apparitions of 4 short period comets (2P, 45P and 96P) are included in this summary and will be the subjects of a future paper and will then be submitted to the PDS. In all three cases the most recent apparitions of these comets were quite similar to the previous ones.

When possible pre- and post-perihelion variations in water production rate have been fitted with a power-law of the form $Q = Q_1 \, r^p$., where Q_1 is the value at a heliocentric distance of 1 AU, r is the heliocentric distance in AU and p is the power-law exponent, to which we often refer as "slope," but this slope is not directly related directly to slopes in visual light curves. Some comets never reached a heliocentric distance of 1 AU and were either always closer or farther away, so the comet never actually had a production rate at 1 AU. In these cases the 1 AU extrapolated value is given anyway. In a few cases such a fit was not possible for a number of reasons. In some cases observational geometry prevented enough measurements to be made either before or after perihelion. In other cases the variation was too irregular for a power-law to have any physical meaning. An example of this would be

a comet where the seasonal effects dominate the variation over time. In other cases the range of heliocentric distance obtained was not large enough for a meaningful power law to be obtained. For 3 long-period comets we provide a mean value at 1 AU for pre- and/or post-perihelion but not a power-law for the reasons stated above. These are C/2001 OG108 (LONEOS), C/2002 G3 (SOHO), and C/2002 O4 (Hoenig).

The error bars for the fitted slopes are given in the appropriate tables. Formal error bars for the fitted production rates are all quite small ranging between 1% and 5%. These are comparable to the individual uncertainties for each production rate given in the PDS tables of individual images and are indicative of internal systematic error resulting from the model fitting, background subtraction procedure and stochastic noise in the SWAN brightness. These are also indicative of the relative uncertainties comparing different SWAN water production rates with one another. On the other hand absolute values of active areas have uncertainties as large as the uncertainties in our production rates, owing to uncertainties in model parameters such as molecular lifetimes, the intensity calibration of SWAN, uncertainty in the adopted absolute value of the solar flux from the LASP web site that contributes to the Lyman-alpha fluorescence used and the 6±3% uncertainty (Combi et al., 2005) coming from other sources of H atoms. Altogether we normally give an approximate absolute uncertainty to water production rates as ±30%. This would be indicative of comparisons of our water production rates with those determined by other observations, such as ground-based IR observations of H_2O, ground-based or space-based observations of OH or radio observations of OH. Because of the large ranges of values in the figures, most of the error bars are comparable to or smaller than the sizes of the data points.

For some short period comets of multiple apparitions it is clear that there is not much overall change from apparition to apparition, e.g. 2P, 21P, 45P, 46P and 96P. Data from multiple apparitions were taken together for calculating power-law variations with heliocentric distance. In section 4 below

these are compared with comets 19P, 55P and 141P that were only observed for one apparition each for purposes of correlation analyses.

For dynamical classification we have adopted the criteria given in the photometric survey study of A'Hearn et al. (1995) that is based on the value of the original semi-major axis (a_0) of each comet. These values were determined from two sources: the JPL Horizons web site and the Minor Planet Center web site. A'Hearn et al. (1995) used values provided by Brian Marsden of the Minor Planet Center. The Minor Planet Center (MPC) provides values of a_0 for most of the comets. With the JPL Horizons tools one can calculate the osculating orbital elements at any desired date. For this work we picked a date of 1950.0 where all the comets in the survey were well past 50 AU on their inbound orbits and long before any influence of Neptune. In most cases the numerical values of a_0 from the two sources were well within 10% of one another. For these we simply give the average of the JPL and MPC values. In a few cases a_0 was very large, or more appropriately the calculated $1/a_0$ was very close to zero or even slightly negative (hyperbolic). It is expected that most hyperbolic orbits resulted from a stellar or planetary perturbations and not indicating original extra-solar comets. However, such comets would eventually leave the solar system. In a couple of cases either there was no MPC value so we give only the JPL Horizons value. When there was some difference in the numerical value of a_0 between the two sources, the dynamical class was still the same.

The A'Hearn et al. dynamical classes are defined as follows:

DN - dynamically new: $a_0 > 20000$ AU; $1/a_0 < 50\times10^{-6}$

YL - young, long period: 20000 AU $> a_0 > 500$ AU; $50\times10^{-6} < 1/a_0 < 2000\times10^{-6}$

OL – old, long period: $a_0 < 500$ AU; $1/a_0 < 2000\times10^{-6}$

JF - Jupiter family $2.0 < T_J < 3.0$

HF - Halley family $T_J > 2.0$

where a_0 is the original semi-major axis for long period comets before entering the planet region of the

solar system, $T_J = \frac{a_J}{a} + 2\sqrt{\frac{a}{a_J}(1-e^2)}\,cos\,i$, is the Tisserand constant with Jupiter, a_J is the semi-

major axis of Jupiter, a, e and i are the semi-major axis, eccentricity and inclination of the comet orbit,

respectively. While the dynamically new class is based on a large original semi-major axis, A'Hearn et

al. (1995) point out that this only means there is a 90% chance of a comet so classified is really on its

first trip into the inner solar system. By the same token other long period comets, YL or OL, could

have been only through the outer solar system previously and had their orbits changed to a smaller

values of a_0 but did not have a small enough perihelion distance to receive significant solar processing.

Therefore, all dynamical classifications are necessarily probabilistic and not an exact indication of past

thermal evolution.

Similarly, it is important to stress that the pre- and post-perihelion power-law results here also

need to be understood only as ensemble properties of various populations of the comets observed and

are indicative of a wide variety of physical responsible for cometary activity. For any individual comet,

the pre- and post-perihelion power-laws could be heavily influenced by peculiar geometrical factors

such as the angle between the spin axis and the orbital axis yielding seasonal effects owing to solar

illumination patterns. Comet 17P/Holmes, for example, was only observed in 2007 in the aftermath of

a huge outburst (Combi et al. 2007) and so a power-law variation with heliocentric distance makes

little sense. Results from the Rosetta mission to comet 67P/Churyumov-Gerasimenko have shown that

nucleus activity and its variation with heliocentric distance might very well be influenced by diurnal

variations as the solar heat wave penetrates to different depths and by moderate scale changes in the

surface due to refreshing of more icy vertical surfaces after mass wasting falls.

De Sanctis et al. (2015) have shown the deposition of surface and/or near surface ice from

infrared spectra obtained with the Rosetta VIRTIS spectrometer as regions of the comet rotate into

darkness but at depth warmer areas continue to sublimate leaving more water closer to the surface. When the region returns into sunlight on the next rotation the water signature decreases in an hour indicating that the water then sublimates away. Similarly, but on a much larger scale, Fornasier et al. (2016) have shown from multicolor imaging of 67P with the Rosetta OSIRIS camera that the nucleus is overall "bluer" near perihelion than farther from perihelion indicating that the surface layers are enriched with water ice near perihelion when the heat wave penetrates much deeper. This might explain why the overall heliocentric distance variation of 67P is so steep, having a slope of -4.5 (Fougere et al. 2016a and 2016b).

Images of the surface of 67P obtained by the Rosetta OSIRIS camera show the continuous evolution of a complex surface with evidence of activity on steeper vertical cliffs and the resulting material falls at the bottom of the cliffs. Vincent et al. (2016) have suggested that cometary dust jets actually result from activity on vertical fractured cliffs as well as in depressions because material can fall rather than leaving a covering dust mantle that could insulate those regions on the surface. Based on the increased solar insolation exposure of the southern hemisphere the difference in steep slope structures between the northern and southern hemispheres have been quantified by Vincent et al. (2017). Even at larger heliocentric distance evidence for similar surface reprocessing in the form of ice and rock flow and fall has been very recently reported by Raponi et al. (2018) at the surface of Ceres by the Dawn spacecraft.

3. SOHO/SWAN Survey Results – Long Period Comets

Table 1 contains the observational circumstances, dynamical classes and water production rate power-law results for 42 long-period comets observed by SWAN and analyzed over the past 20 years. The dataset is based on over 2600 images. Several comets were observed for a year or more with over

100 observations each, e.g. C/1995 O1 (Hale-Bopp), C/2001 Q4 (NEAT), C/2009 P1 (Garradd), C/2012 Q2 (Lovejoy), etc. Some others are represented by only a handful of images.

Figure 3 shows the pre-perihelion slopes as a function of the inverse original semi-major axes for the entire set of long-period comets. Figure 4 shows the post-perihelion slopes as a function of the inverse original semi-major axes for the entire set of long-period comets. In both cases comets with very large semi-major axis and conversely very small inverse semi-major axis are all plotted just to the right of the plot at $a_0 = 60000$ AU, because the uncertainties in inverse semi-major axis are large. Figure 3 clearly shows a difference in pre-perihelion power-law slopes as a function of dynamical classes. The broadest variation in slopes ranging to values as low as -8 is confined to the OL class and being consistent with the most evolution. For those in the DN class slopes typically are in the range of -3 to -1. Those in the YL class are generally intermediate in range of slopes between the OL and DN classes. The behavior is consistent with a gradual steepening of the water production rate variation slope with age.

Figure 5 shows a scatter-correlation plot of pre-perihelion slope versus post-perihelion slope. There is no obvious correlation between the two. The main difference is that except for comet C/2014 Q1 (PanSTARRS) with both slopes being very steep at -7.8 and -8.9, the majority of pre-perihelion slopes cover a somewhat narrower range than do the post-perihelion slopes. Note that the lower limit of the post-perihelion slope does not include comet C/1999 S4 (LINEAR) at -19.6 resulting from its total disintegration beginning very near perihelion. It's very flat pre-perihelion slope of -1.2 as well as its very large original semi-major axis are consistent with it having been truly dynamically new and on its first trip into the inner solar system.

4. SOHO/SWAN Survey Results – Short Period Comets

Table 2 gives the observational and orbital aspects and parameters of each of the short period comet apparitions that were observed by the SOHO SWAN instrument since launch in December 1995. As can be seen from the value of the Tisserand constant with Jupiter and the classification definition given in the previous section of this paper, all of the comets are Jupiter Family with the exceptions of 55P/Tempel-Tuttle, 8P/Tuttle and 96P/Machholz 1. All these are well-known exceptions with 8P/Tuttle and 55P/Tempel-Tuttle being Halley Family comets and 96PMachholz 1 being a possibly captured Oort cloud or even extra-solar comet (Schleicher 2008). Unlike some previous comet survey papers, we did not include population histograms of quantities such as inclination, Tisserand constant, or perihelion, because the results are not particularly illuminating.

Table 3 gives observational results of the individual apparitions of short period comets including the power-law fits to pre- and post-perihelion parts of the orbit when available and appropriate as well the pre- and post-perihelion active areas from the production rate at 1 AU using the method of Cowan and A'Hearn (1979) for a rotating nucleus. Table 4 gives a reduced set of short period comet results where the power-law fits for five multiple apparition comets have been taken together as well as where nucleus radii have been determined. We did not include comets 41P, 46P, or 73P, which show considerable variation from apparition to apparition.

The trends of pre- or post-perihelion power law slopes with the short period comets' perihelion distance are weak. One might expect if increasing slope were a sign of evolution that the comets with smaller perihelion distances might tend to have steeper slopes, but the perihelion distance and slope are not correlated. In Figure 6 there is no obvious trend of pre-perihelion power-law slope with the perihelion distance. In Figure 7 there is a slight downward trend of post-perihelion power-law slope with the perihelion distance, but it is difficult to conclude it is significant. The short period comets in Figures 6 and 7 include multiple apparition comets (Table 4), which seem consistent over the apparitions covered, and single apparition comets, where there was a reasonable power-law fit.

The same cannot be said about the active fraction, however. For the short period comets where there are measured values of the radius, it is possible to calculate the active fractional area of the comet by using the Cowan and A'Hearn (1979) method for calculation of the active area assuming a rapidly rotating nucleus and the power-law fitted production rate at 1 AU, and dividing by $4\pi r_N^2$, where r_N is the radius of the comet, and water-driven sublimation from a dark nucleus. Errors in active fraction are driven by uncertainties in water production rates, determined nucleus radii, and the appropriateness of the Cowan and A'Hearn (1979) sublimation models used. Published nucleus radii are determined by one or more of several methods (Lamy et al. 2004): photometry of bare nuclei at large heliocentric distance, combinations of visual photometry and thermal infrared flux, radar cross sections, and spacecraft flyby imaging.

Figures 8 and 9 show plots of the active fraction plotted against each comet's perihelion distance for the pre-perihelion and post-perihelion power-laws, respectively. For the comets that appear in Figures 8 and 9 we include error estimates in the notes to Table 3 that come from the original published papers or the mean of several published measured values. Comets 8P and 41P have radar cross sections. Radii of comets 19P, 67P and 103P have been determined by several methods but were verified in spacecraft flyby images. Radii of comets 2P and 21P were determined by traditional ground-based methods but have quite small uncertainties of ± 0.3 and 0.05 km, respectively. The radius of comet 96P was also determined by traditional ground-based optical methods but Lamy et al. (2004) gives three very similar values of 3.5, 2.8 and 3.2 km which yield a mean error of ± 0.2 km. Similarly, 46P which was the original Rosetta mission target comet has values of 0.62, 0.56, 0.7 and 0.6 km as well as some much larger upper limits. The average of 0.6 km has a mean uncertainty of ± 0.04 km. The two most uncertain are comet 41P with an optical value of 0.7 km and a lower limit of > 0.45 km from radar by Howell et al. (2017). Therefore for most of the comets in Figure 8 and 9 the uncertainties in radius are in the range of up to 20% which would yield an additional uncertainty to the active

fraction of up to ~40%. Since the range of abscissae in Figures 8 and 9 cover three orders of magnitude the apparent trends are quite valid even accounting for all sources of uncertainty. For both pre- and post-perihelion cases there are clear and obvious trends of small active fractions for small perihelion distances. This could very well be consistent with the increased solar exposure of comets with smaller perihelion distances on each orbit gradually decreasing the near surface coverage of sublimating ice and thus lowering activity levels per unit surface area.

5. Compositional Taxonomic Classes

Table 5 gives the standard ground-based carbon species taxonomic classifications of the set of comet observed by SWAN, namely typical and depleted. For this we have combined classifications found in the papers by A'Hearn et al. (1995), Fink and Hicks (1996), Fink (2009), Cochran et al. (2012), and a recent reclassification of visual ground based results from various published data by Dello Russo et al. (2016). The comprehensive multi-level classification of parent molecules in the infrared by Dello Russo et al. (2016) does not have enough comets in common with the SWAN set to make a meaningful comparison. Classification for C/2009 R1 (McNaught) was taken from the observations of Korsun et al. (2012) and that for C/2014 Q2 (Lovejoy) was taken from the observations of Venkataramani et al. (2016). Table 5 shows the SWAN comets for which typical and depleted classifications can be inferred by measurements of C_2, CN and OH.

Table 6 shows pre- and post-perihelion slopes comparing short period, typical and depleted comets and long period, typical and depleted comets. Unfortunately, the averages are limited by small number statistics. There are some trends, however. First, in each taxonomic class there is no significant difference between pre- and post-perihelion populations of each, so in Table 6 we averaged pre- and post-perihelion slopes to increase the sampling set. Perhaps surprisingly for long-period comets the depleted comets had shallower average power-law slopes than did the typical comets. The depleted

short period comets had steeper slopes on the average than the typical short period comets. In additions, not surprisingly, the short period comets had steeper average power-law slopes than long period comets in general. For the comparison of long and short period comets the same trend was seen in the photometric survey of A'Hearn et al. (1995).

6. Summary and Conclusions

The photometric composition survey of A'Hearn et al. (1995) provided a comparison of a limited number of production rate power-law exponent dependencies for OH, CN C_2, C_3 and NH, where OH can be considered a reasonable proxy for H_2O. For OH they found a trend of steeper negative slopes going from Dynamically New pre-perihelion, Dynamically New post-perihelion Young Long-Period, Old Long-Period, Halley Family, Jupiter Family typical, and Jupiter Family depleted. In these cases their power-law exponents were generally only determined from a few points at different heliocentric distance. Our results shown in Figures 8 and 9 are consistent with the trend of the median values shown by A'Hearn et al. but having many more samples determined from wider and higher sampled production rate values shows the details are more complicated. We show a much wider range of slopes for long period comets with smaller original semi-major axes that would be classified as Old Long Period and a narrow range for those with large original semi-major axes that would be classified as Dynamically New or Young Long Period. We do see an average difference between pre- and post-perihelion dynamically new comets, but having more samples shows there is still a considerable range in values about the mean or median.

For the short-period comets where nucleus radii have been determined there is a clear and consistent trend of larger active fractional area with larger perihelion distance. This would be consistent with an evolutionary trend of more processing for the comets with smaller perihelion distance caused by the larger orbit-integrated solar insolation. There is, however, little correlation of power-law slope

16

with perihelion distance. For the long-period comets the main evolution trend is that the Old Long Period comets have a much wider range of power-law slopes than to Dynamically New or Young Long Period comets.

A possible difference in the manifestation of the evolutionary changes between short-period and long-period comets could be at what stage the evolution happened. The main effect of solar exposure on long-period comets we see likely happens on the comets' first or first couple of passes into the inner solar system. This is when the primordial surface layers that have long been at large distances from the sun are first sublimated away. In SWAN survey results there is both a small but significant difference in the pre- and post-perihelion power-law slopes as well as most clearly a change in the range of power-law slopes in progressing from the Dynamically New to Young Long Period and finally to Old Long Period. Because of their short periods most short period comets had their first pass or two in the inner solar system at least several passes ago and fell into whatever their slopes are based mostly on seasonal effects and distribution of active regions on the surface. The evolutionary trend of smaller active fractional areas with smaller perihelion distances is possibly seen after many more orbits around the sun. The original more primordial surface layers of short period comets coming from the Kuiper belt are likely burned off after the first pass through the inner solar system upon capture by Jupiter.

Comparisons of power-law slopes with compositional taxonomic classes are complicated by the more limited overlap in comets observed by SWAN and those that have been classified by compositional surveys especially for the long-period comets. Even though there was difference between the distribution of pre- and post-perihelion slopes for the whole long-period comet set, for those which have a taxonomic classification there was no significant difference in pre- and post-perihelion slopes, so both were averaged together for the purpose of comparison here. In this case the depleted long-period comets had shallower slopes than the typical long-period comets. This could be simply a difference with no evolutionary cause. For the short period comets that have been classified

by composition, the comparison was the opposite where the depleted short-period comets had steeper slopes than the typical short-period comets. It has been suspected that chemical depletion of volatile species may have no consistent evolutionary trend or show a difference between Oort cloud (long period) and Kuiper Belt (short period) origin (Mumma and Charnley 2011; Dello Russo et al. 2016). There is nothing in the results contained in the SWAN survey that goes against this idea; however there do seem to be consistent trends in power-law slopes and active fraction that are related to the evolution of the cometary nucleus.

References

A'Hearn, Michael F., Millis, Robert C., Schleicher, David G., Osip, David J., Birch, Peter V. 1995. The ensemble properties of comets: Results from narrowband photometry of 85 comets, 1976-1992. Icarus, 118, 223-270, doi:10.1006/icar.1995.1190.

Bertaux, J. L., 2015. Estimate of the erosion rate from H_2O mass-loss measurements from SWAN/SOHO in previous perihelions of comet 67P/Churyumov-Gerasimenko and connection with observed rotation rate variations. Astron. Astrophys, A&A 583, A38 DOI: 10.1051/0004-6361/201525992

Bertaux, J. L., Kyrölä, E., Quémerais, E., Pellinen, R., Lallement, R., Schmidt, W., Berthé, M., Dimarellis, E., Goutail, J. P., Taulemesse, C., Bernard, C., Leppelmeier, G., Summanen, T., Hannula, H., Huomo, H., Kehlä, V., Korpela, S., Leppälä, K., Strömmer, E., Torsti, J., Viherkanto, K., Hochedez, J. F., Chretiennot, G., Peyroux, R., Holzer, T. 1995. SWAN: A Study of Solar Wind Anisotropies on SOHO with Lyman Alpha Sky Mapping. Solar Physics, 162, 403-439, doi:10.1007/BF00733435

Bertaux, J. L., Costa, J., Quémerais, E., Lallement, R., Berthé, M., Kyrölä, E., Schmidt, W., Summanen, T., Makinen, T., & Goukenleuque, C. 1998. Lyman-alpha observations of comet Hyakutake with SWAN on SOHO. Planet. Sp. Sci. 46, 555-568, doi:10.1016/S0032-0633(97)00179-7.

Bockelee-Morvan, D. and Crovisier, J., 1987 The role of water in the thermal balance of the coma. In ESA, Proceedings of the International Symposium on the Diversity and Similarity of Comets p 235-240.

Boehnhardt, H., Rainer, N., Birkle, K., Schwehm, G. 1999. The nuclei of comets 26P/Grigg-Skjellerup and 73P/Schwassmann-Wachmann 3. Astron. Astrophys. 912-917.

Cochran, A.L., Barker, E.S., Gray, C.L. 2012. Thirty years of cometary spectroscopy from McDonald Observatory. Icarus 218, 144-168.

Combi, M.R., 1989,.The outflow speed of the coma of Halley's comet. Icarus 81, 41-50.

Combi, M. 2017. SOHO SWAN Derived Cometary Water Production Rates Collection, urn:nasa:pds:soho:swan_derived::1.0, L. Feaga (ed), NASA Planetary Data System.

Combi, M. R., Harris, W. M., Smyth, W. H. 2004. Gas dynamics and kinetics in the cometary coma: theory and observations. In Comets II, M. C. Festou, H. U. Keller, and H. A. Weaver (eds.), University of Arizona Press, Tucson, 745 pp., p.523-552.

Combi, M. R., Boyd, Z., Lee, Y., Patel, T. S., Bertaux, J.-L., Quémerais, E., Mäkinen, J. T. T. 2011a. SOHO/SWAN observations of comets with small perihelia: C/2002 V1 (NEAT), C/2002 X5 (Kudo-Fujikawa), 2006 P1 (McNaught) and 96P/Machholz 1. Icarus, 216, 449-461, doi:10.1016/j.icarus.2011.09.019.

Combi, M. R., Fougere, N., Mäkinen, J. T. T., Bertaux, J.-L., Quémerais, E., Ferron, S. 2014. Unusual Water Production Activity of Comet C/2012 S1 (ISON): Outbursts and Continuous Fragmentation. Astrophys. J. Lett.,788:L7, doi:10.1088/2041-8205/788/1/L7.

Combi, M. R., Lee, Y., Patel, T. S., Mäkinen, J. T. T., Bertaux, J.-L., Quémerais, E. 2011b. SOHO/SWAN Observations of Short-period Spacecraft Target Comets. Astron. J., 141:128, doi: 10.1088/0004-6256/141/4/128.

Combi, M.R., Bertaux, J.-L., Quémerais, E., Ferron, S. 2011c. Water Production by Comet 103P/Hartley 2 Observed with the SWAN Instrument on the SOHO Spacecraft. Astrophys. J. (Lett.) 734:L6.

Combi, M.R. J.T.T. Mäkinen, J.-L. Bertaux, & E. Quémerais. 2005, Temporal deconvolution of the hydrogen coma. II. Pre- and post-perihelion activity of Comet Hyakutake. (1996 B2) Icarus. 177, 228-245, doi: 10.1016/j.icarus.2005.03.007.

Combi, M.R., J.T.T. Mäkinen, J.-L. Bertaux, E. Quémerais, S. Ferron. 2007. Comet 17P/Holmes. IAU Circ, No. 8905, #1. Edited by Green, D.W.E.

Combi, M.R., J.T.T. Mäkinen, J.-L. Bertaux, E. Quémerais, S. Ferron, N. Fougere. 2013. Water production rate of Comet C/2009 P1 (Garradd) throughout the 2011-2013 apparition: Evidence for an icy grain halo. Icarus, 225, 740-748, doi: 10.1016/j.icarus.2013.04.030.

Combi, M.R., J.T.T. Mäkinen, N.J. Henry, J.-L. Bertaux and E. Quémerais. 2008. SOHO/SWAN Observations of Five Moderately Bright Comets: 1999-2002. *Astron. J.* 135, 1533-1550.

Combi, M. R., Reinard, A. A., Bertaux, J.-L., Quemerais, E., Mäkinen, T. 2000. SOHO/SWAN Observations of the Structure and Evolution of the Hydrogen Lyman-α Coma of Comet Hale-Bopp (1995 O1). Icarus, 144, 191-202, doi:10.1006/icar.1999.6335.

Combi, M.R., Smyth, W.H., 1988a. Monte Carlo particle trajectory models for neutral cometary gases. I. Models and equations. Astrophys. J. 327, 1026–1043.

Combi, M.R., Smyth, W.H., 1988b. Monte Carlo particle trajectory modelsfor neutral cometary gases. II. The spatial morphology of the Lyman alpha coma. Astrophys. J. 327, 1044–1059

Cowan, J. J., A'Hearn, M. F. 1979. Vaporization of comet nuclei - Light curves and life times. Moon & Planets, 21, 155-171, doi:10.1007/BF00897085.

Crovisier, J., Colom, P. Gérard, E., Bockelée-Morvan, D., Bourgois, G. 2002. Observations at Nançay of the OH 18-cm lines in comets. The data base. Observations made from 1982 to 1999. Astron. Astrophys. 393, 1053-1064.

De Sanctis, M.C. and 23 colleagues. 2015. The diurnal cycle of water ice on comet 67P/Churyumov-Gerasimenko. Nature 525, 500-503.

Dello Russo, N., Kawakita, H., Vervack Jr., R.J., Weaver, H.A. 2016. Emerging trends and a comet taxonomy based on the volatile chemistry measured in thirty comets with high-resolution infrared spectroscopy between 1997 and 2013. Icarus 278, 301-332.

Fernandez, Y.R., Lisse, C.M., Ulrich, K.H., Peschke, S.B., Weaver, HA, A'Hearn, M.F., Lamy, P., Livengood. T.A., Kostiuk. 2000. T. Physical properties of the nucleus of comet 2P/Encke. Icarus147, 145-160.

Fernandez, Y.R., Kelley, M.S., Lamy, P.L., Toth, I., Groussin, O., Lisse, C.M., A'Hearn, M.F., Bauer, J.M., Campins, H., Fitzsimmons, A., Licandro, J. Lowry, S.C., Meech, K.J., Pittichová, J., Reach, W.T., Snodgrass, C., Weaver, H.A. 2013. Thermal properties, sizes and size distribution of Jupiter-family cometary nuclei. Icarus 226, 1138=2270.

Festou, M.C. 1981. The density distribution of neutral compounds in cometary atmospheres. I - Models and equations. Astron. Astrophys. 95, 69-79.

Fink, U., Hicks, M.D. 1996. A survey of 39 comets using CCD spectroscopy. Astrophys. J. 459, 729-743.

Fink, U. 2009. A taxonomic survey of comet composition 1985-2004 using CCD spectroscopy. Icarus 201, 311-334.

Fink, U., Combi, M.R. 2004. The effect of using different scale lengths on the production rates of Comet 46P/Wirtanen. Plan. Sp. Sci. 52, 573-580.

Fornasier, S. and 52 colleagues. 2016. Rosetta's comet 67P/Churyumov-Gerasimenko sheds it dusty mantle to reveal its icy nature. Science 354, 1566-1570.

Fougere, N. and 28 colleagues, 2016a. Three-dimensional direct simulation Monte-Carlo modeling of the coma of comet 67P/Churyumov-Gerasimenko observed by the VIRTIS and ROSINA instruments on board Rosetta. Astron. Astrophys. 588, id.A134 (11 pp.).

Fougere, N. and 28 colleagues, 2016b. Direct Simulation Monte Carlo modelling of the major species in the coma of comet 67P/Churyumov-Gerasimenko. Mon. Not. Roy. Astr. Soc. 462S, S156-S169.

Harmon, J.K., Nolan, M.C., Giorgini, J.D., Howell, E.S. 2010. Radar obervations of 8P/Tuttle: A contact-binary comet. Icarus 207, 499-502.

Harmon, J.K., Nolan, M.C., Howell, E.S., Giorgini, J.D. 2008. Comet 8P/Tuttle. IAUC 8909, edited by Green, D.W.E.

Howell, Ellen S., Lejoly, Cassandra, Taylor, Patrick A., Rivera-Valentin, Edgard G., Zambrano-Marin, Luisa Fernanda, Giorgini, Jon D., Nolan, Michael C., Samarasinha, Nalin H., Mueller, Beatrice E. A., Aponte-Hernandez, Betzaida, Saran Bhiravarasu, Sriram, Rodriguez Sanchez-Vahamonde, Carolina, Harris, Walter M. Arecibo radar observations of 41P/Tuttle-Giacobini-Kresák constrain the nucleus size and rotation. American Astronomical Society, DPS meeting #49, id.414.24, 2017.

Keller, H.U., Meier, R.R. 1976. A cometary hydrogen model for arbitrary observational geometry. Astron. Astrophys. 52, 273-281.

Korsun, Pavlo, IrinaKulyk, Sergey Velichko. 2012. The spectrum of comet C/2009R1(McNaught) in 4140–5240 Å wavelength region. Planet. Sp. Sci. 60, 255-260.

Langland-Shula, L.E., Smith, G.H. 2011. Comet classification with new methods for gas and dust spectroscopy. Icarus 213, 280-322.

Lamy, P.L., Toth, I., Jorda, Weaver, H.A., A'Hearn, M.F. 1998 The nucleus and inner coma of comet 46P/Wirtanen. Astron. Astrophys. 335, L25-L29.

Lamy, P.L., Toth, I., Fernandez, Y., Weaver, H.A. 2004. The sizes, shapes, albedos, and colors of cometary nuclei. In Comets II, ed. by Festou, M.C., Keller, H.U., Weaver, H.A., pp. 223-264, U. of Arizona Press, Tucson, Arizona.

Lamy, P.L., Toth, I., A'Hearn, M.F. Weaver, H.A., Jorda, L. 2007. Rotational sate of the nucleus of comet 9P/Tempel 1: Results from Hubble Space Telescope observations in 2004. Icarus, 187, 132-143.

Lamy, P.L Toth, I., Davidsson, B.J.R., Groussin, O. Gutierrez, P., Jorda, L. Kaasalainen, M., Lowry. 2007. A portrait of the nucleus of comet 67P/Churyumov-Gerasimenko. Sp. Sci. Rev. 128, 23-66.

Lamy, P.L., Toth, I, Weaver, H.A. 2014. Hubble Space Telescope observations of the nucleus of comet C/2012 S1 (ISON). Astrophys. J. (Lett.) 794, 9L.

Lisse, C.M., Fernandez, Y.R., Reach, W.T., Bauer, J.M., A'Hearn, M.F., Farnham, T.L., Groussin, O., Belton, M.J., Meech, K.J., Snodgrass, C.D. 2009. Spitzer Space Telescope observations of the nucleus of comet 103P/Hartley 2. Pub. Astron. Soc. Pac. 121, 968-975.

Lowry, S., Fitzsimmons, A., Collander-Brown, S. 2003. CCD photometry of Jupiter-family comets. III. Ensemble properties of Jupiter-family comets. Astron. Astrophys. 297, 329-343.

Mäkinen, J. Teemu T., Combi, Michael R. 2005. Temporal deconvolution of the hydrogen coma I. A hybrid model. Icarus, 177, 217-227, doi:10.1016/j.icarus.2005.02.010.

Mumma, M. J., Charnley, S.B. 2011. The chemical composition of comets -- Emerging taxonomies and natal heritage. Annu. Rev. Astron. Astrophys. 49, 471-524.

Newburn, R.L. Jr., Spinrad, H. 1989. Spectrophotometry of 25 comets: Post-Halley updates for 17 comets plus new observations for eight additional comets. Astron. J. 97, 552-569.

Pittichová, J. Woodward, C.E., Kelley, M.S., Reach, W.T. 2008. Ground-based optical and Spitzer infrared imaging observations of comet 21P/Giacobini-Zinner. Astron. J. 136, 1127-1136.

Raponi, A. and 21 colleagues. 2018. Variations in the amount of water ice on Ceres' surface suggest a seasonal water cycle. Science Advances 4, eaao3757.

Schleicher, D.G., 2008. The extremely anomalous molecular abundances of Comet 96P/Machholz 1 from narrowband photometry. Astron. J. 136, 2204–2213.

Shou, Y., Combi, M.R., Toth, G., Tenishev, V. Fougere, N., Jia, X., Rubin, M., Huang, Z., Hansen, K., Gombosi, T., Bieler, A. 2016. A new 3D multi-fluid model: A study of kinetic effects and variations of physical conditions in the cometary coma. Astrophys. J. 833:160.

Snodgrass, C., Lowry, S.C., Fitzsimmons, A. 2006. Photometry of cometary nuclei: rotation rates, colours and a comparison with Kuiper Belt Objects. Mon. Not. R. Astron. Soc. 373, 1590-1602.

Tancredi, G., Fernández, J.A., Rickman, H., Licandro, J. 2006. Nuclear magnitutdes and the size distribution of Jupiter family comets. Icarus 182, 527-549.

Tseng, W.-L., Bockelée-Morvan, Crovisier, J., Colom, P., Ip, W.-H. 2007. Cometary water expansion velocity from OH line shapes. Astron. Astrophys. 467, 729-735.

Venkataramani, Kumar, Satyesh Ghetiya, Shashikiran Ganesh, U. C. Joshi, Vikrant K. Agnihotri and K. S. Baliyan. 2016. Optical spectroscopy of comet C/2014 Q2 (Lovejoy) from the Mount Abu Infrared Observatory. MNRAS 463, 2137-2144.

Vincent, J.-B. and 54 colleagues. 2016. Are fractured cliffs the source of cometary dust jets? Insight from OSIRIS/Rosetta at 67P/Churyumov-Gerasimenko. Astron. Astrophys. 587, id.A14.

Vincent, J.-B. and 51 colleagures. 2017. Constraints on cometary surface evolution derived from a statistical analysis of 67P's topography. Monthly. Not. Roy. Astron. Soc. 469, S329-S338.

Weaver, H.A., Stern, S.A., Parker, W. 2003. Hubble Space Telescope STIS Observations of comet 19P/Borrelly during the Deep Space 1 Encounter. Astron. J. 125, 444-451.
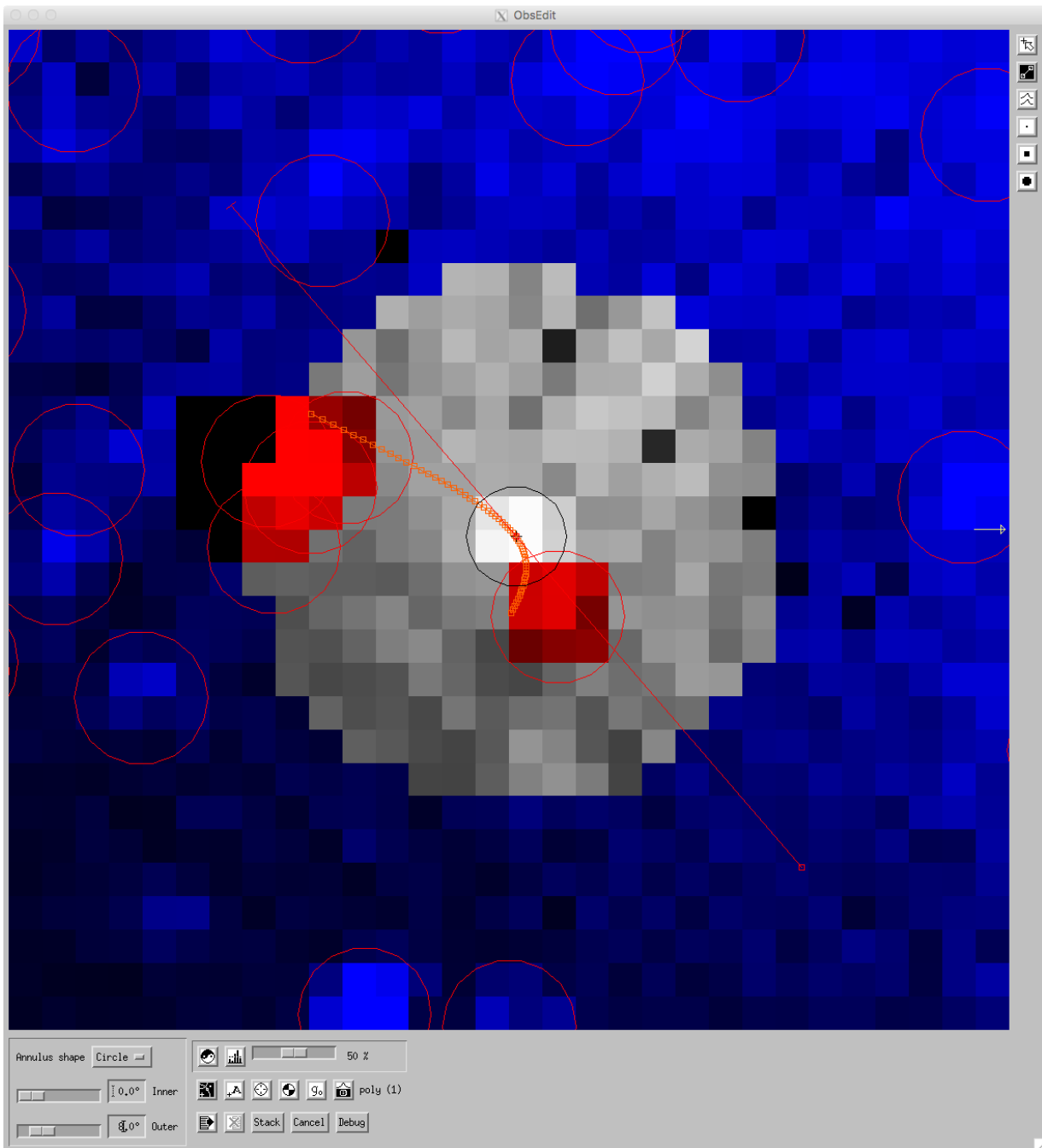
Figure 1. Lyman-α brightness distribution around comet C/2009 P1 (Garradd) on 1 November 2011. The comet is at the center of the image. The analysis is done on circle of radius 8 degrees shown in gray shades. Each small square corresponds to a 1 degree pixel. The blue shades are the sky background, namely the interplanetary medium emission of hydrogen Lya and background stars. The locations of stars are indicated by red circles. Those stars that would interfere with the comet signal are masked and highlighted in red. The red line from upper left to lower right shows the location of the brightness profile shown in Figure 2.
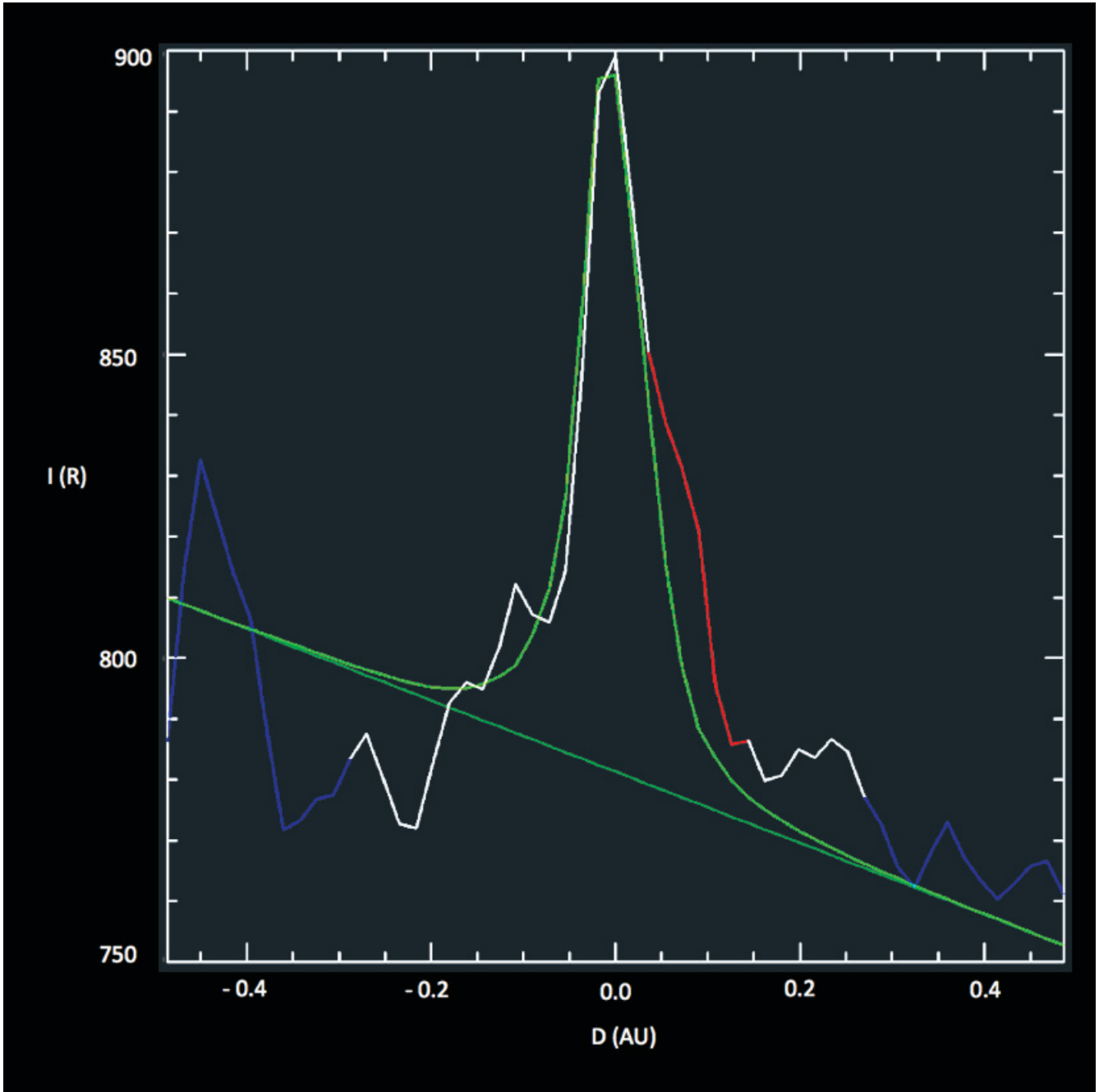
Figure 2. A brightness profile through the position of comet C/2009 P1 (Garradd). The white line indicates the observed brightness distribution. The green peaked profile is the TRM fit to the comet distribution and the green line below is the TRM fit to the IPM background. Red lines indicate the presence of stars that are excluded from the analysis. The blue line is the observed brightness mainly of the background IPM. Brightness is in Rayleighs and distance is in AU.
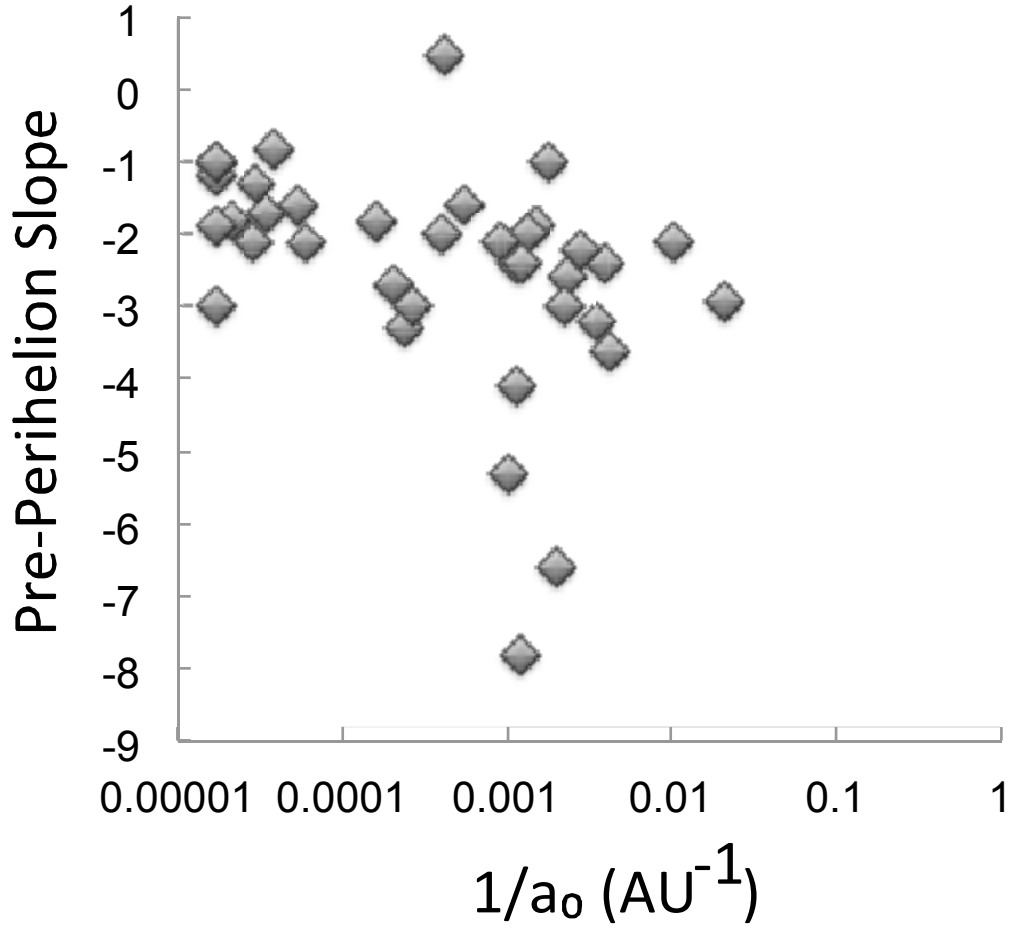
Figure 3. Dependence of the variation of pre-perihelion slopes on long-period comet inverse original semi-major axis.
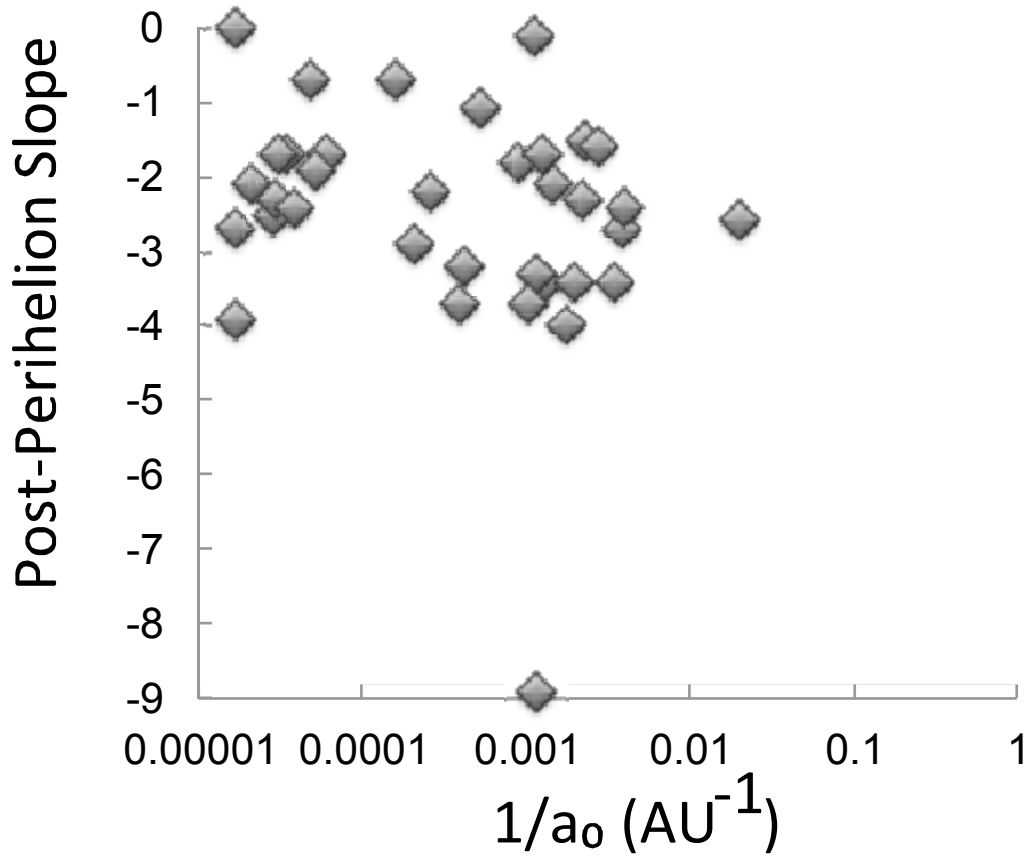
Figure 4. Dependence of the variation of post-perihelion slopes on long-period comet inverse original semi-major axis. The value of the post-perihelion slope for comet C/1999 S4 (LINEAR) is -19.6 and does not appear because it is a special case and for easier direct comparison between Figures 3 and 4.
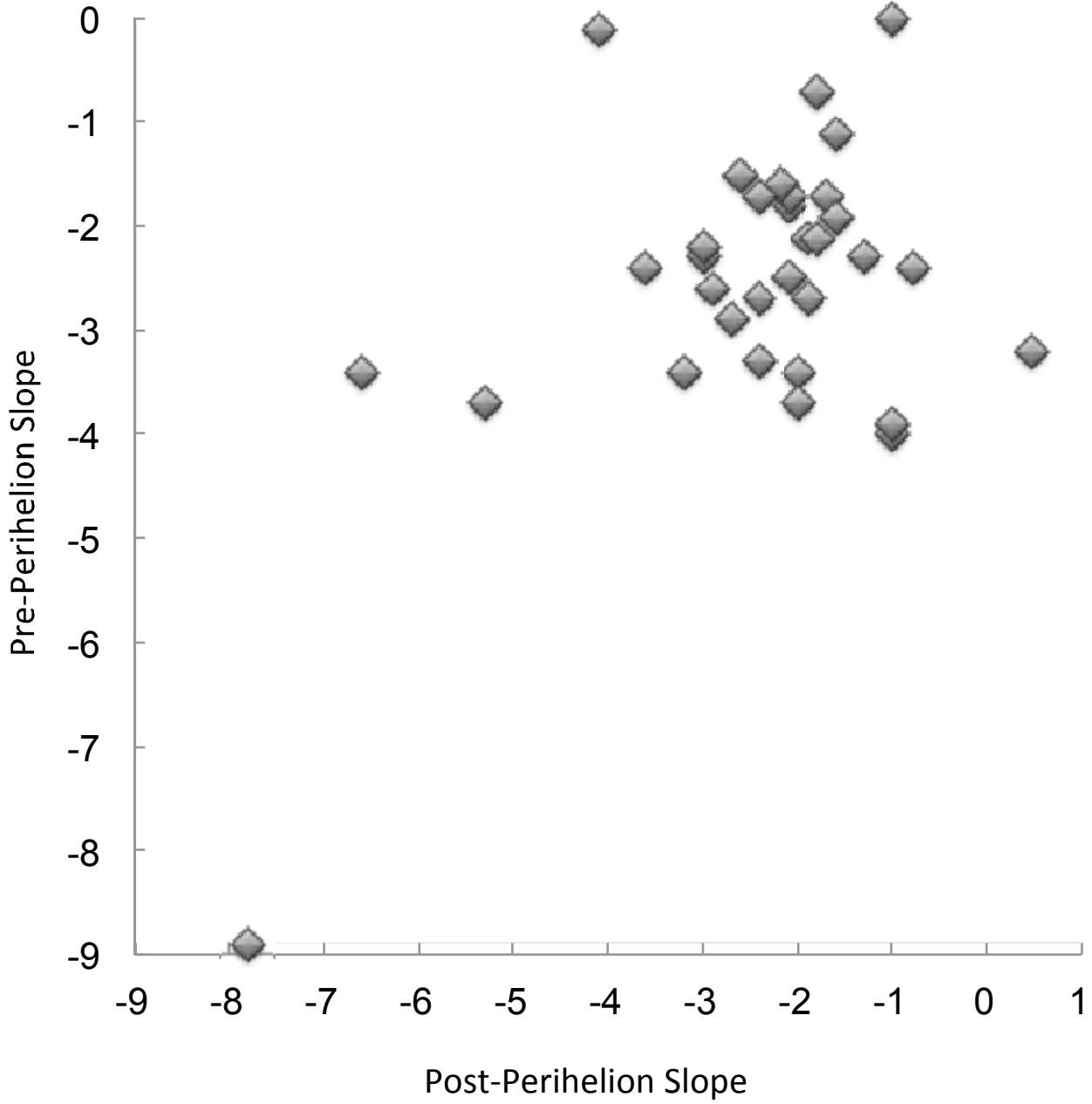
Figure 5. Correlation of pre-perihelion slopes with post-perihelion slopes for long-period comets.
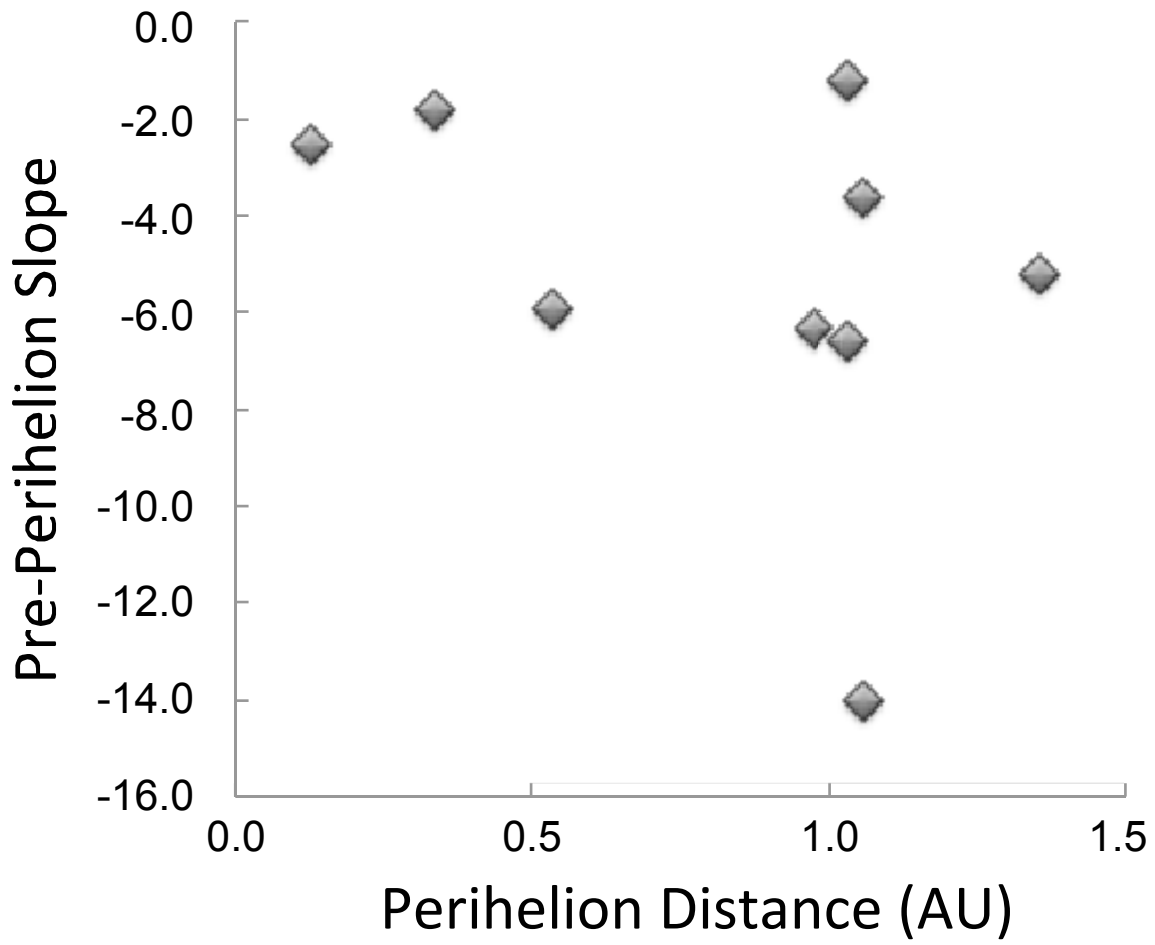
Figure 6. Correlation of pre-perihelion slopes with perihelion distance for short-period comets.
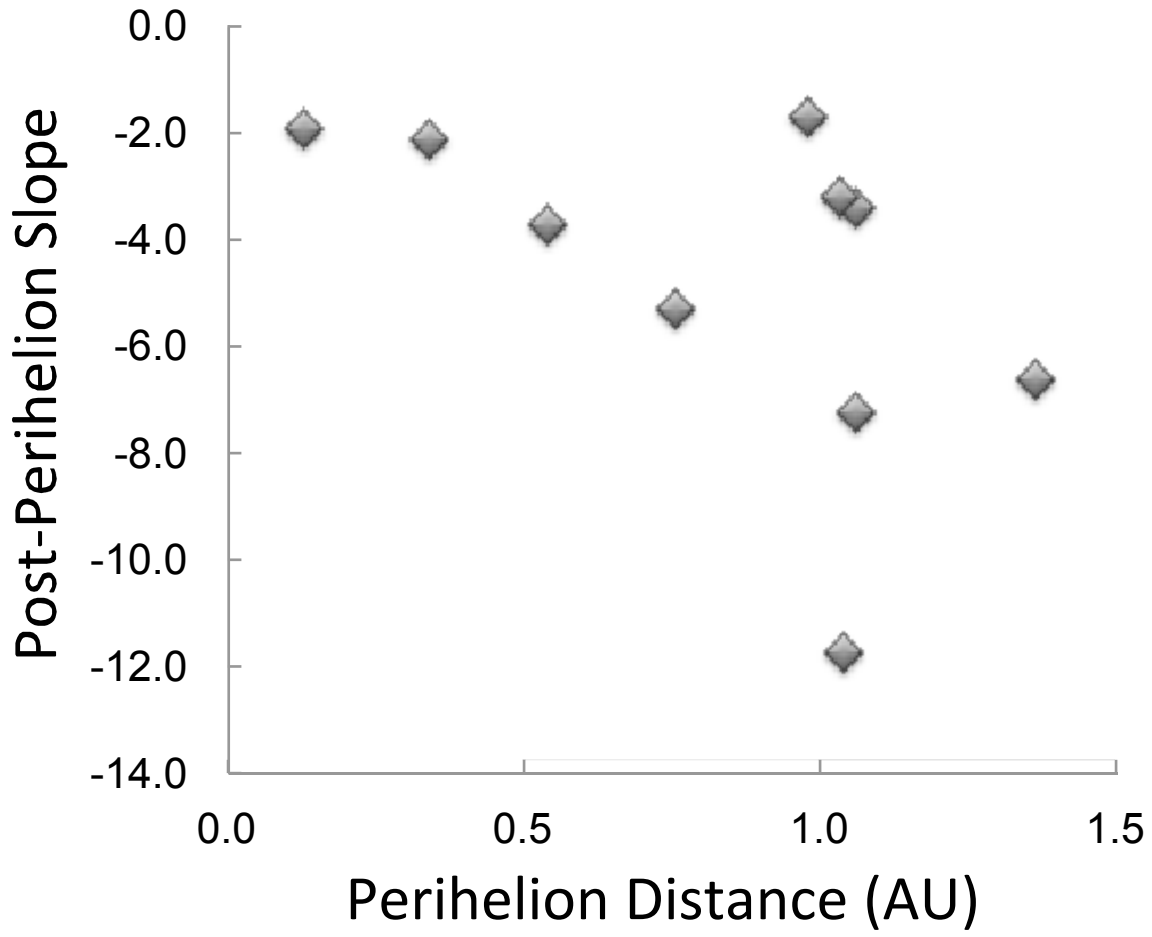
Figure 7. Correlation of post-perihelion slopes with perihelion distance for short-period comets.

Figure 8. Correlation of pre-perihelion active fraction with perihelion distance for short-period comets.

Figure 9. Correlation of post-perihelion active fraction with perihelion distance for short-period comets.

Table 1. Summary of Long-period Comets Observations, Orbital Aspects, and Production Rates

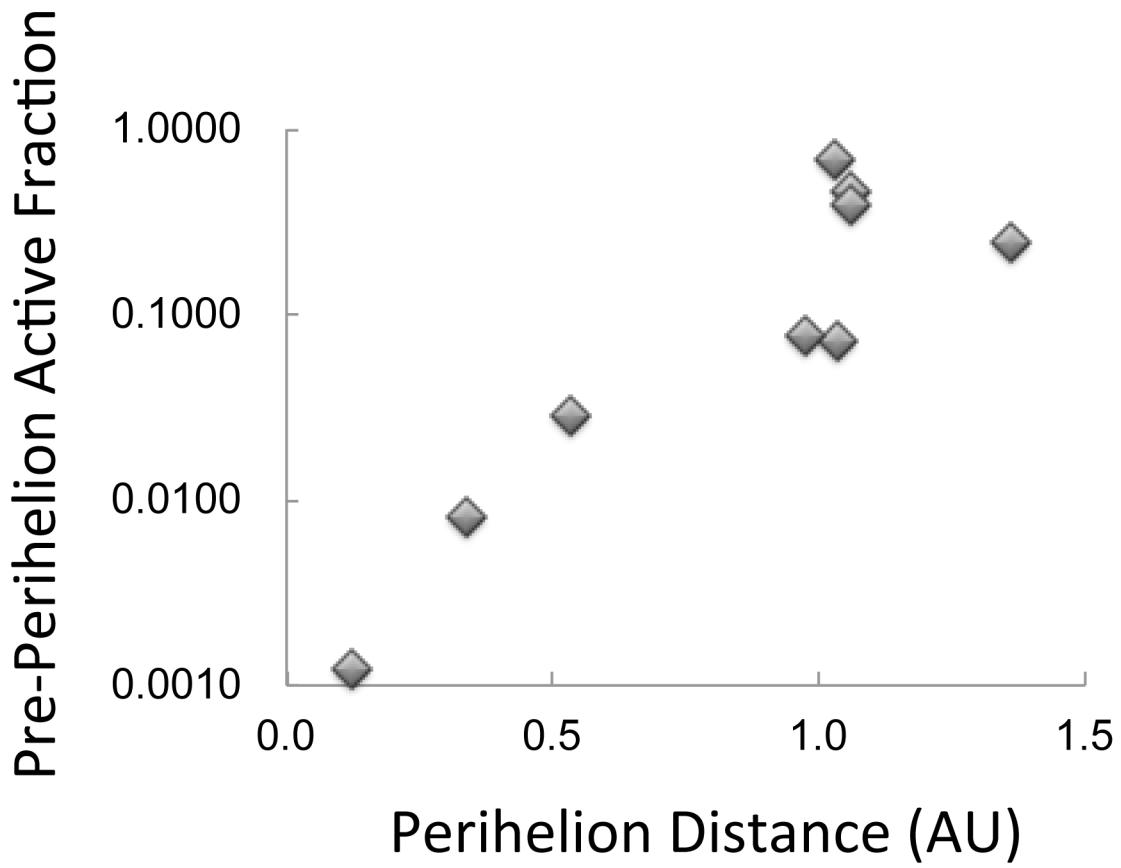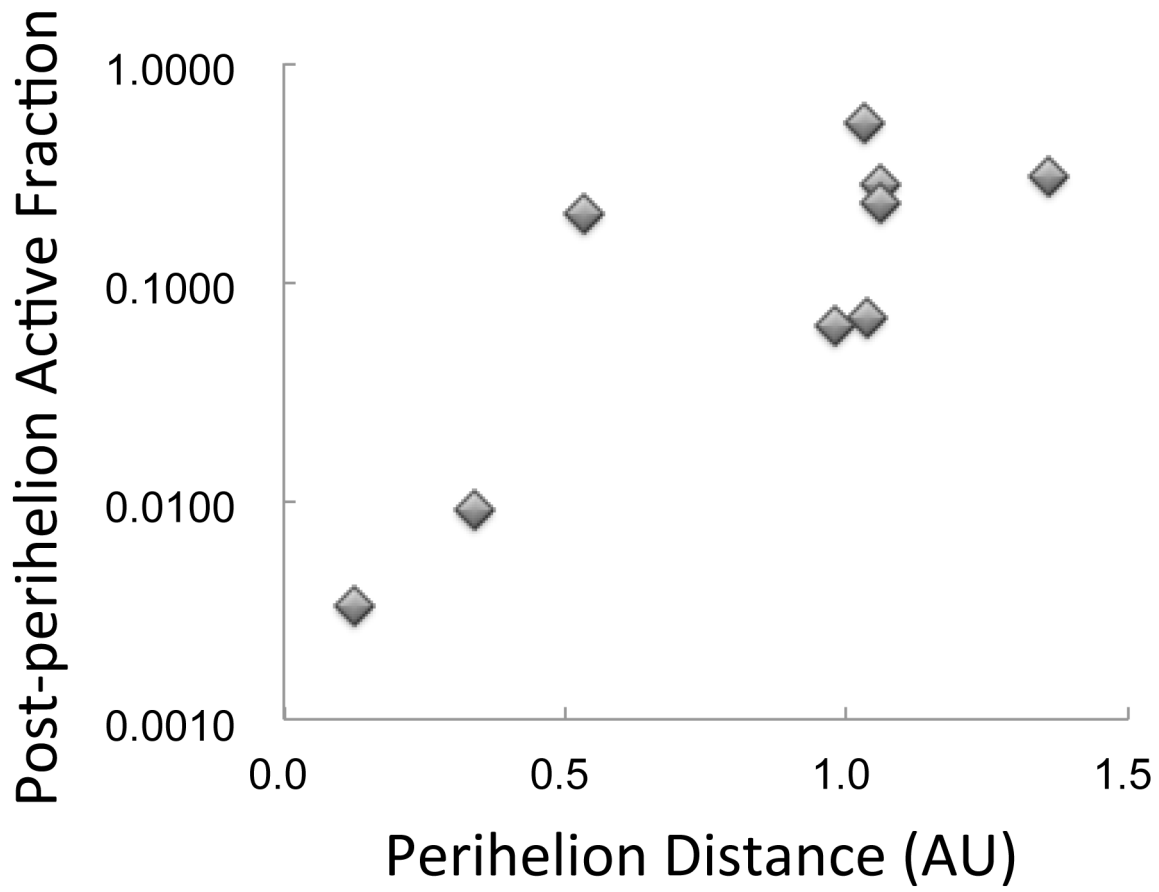| Comet	T-Perihelion	T-Begin	T-End	N	q	$1/a_0$	Class	Q1-pre	p-pre	Q1-post	p-post
C/1996 B2 (Hyakutake)	19960501.3948	-75.60	66.58	63	0.230224	1.52E-03	OL	5.05E+29	-1.9±0.08	4.12E+29	-2.1±0.08
C/1996 Q1 (Tabur)	19961103.5291	-59.535	11.373	32	0.839815	1.80E-03	OL	4.13E+28	-1.0±0.1	5.63E+27	-4.0±2.2
C/1995 O1 (Hale-Bopp)	19970331.2270	-240.124	178.316	142	0.922110	3.82E-03	OL	1.41E+31	-2.4±0.02	1.24E+31	-2.7±0.1
C/1997 O1 (Tilbrook)	19970713.4193	-14.095	30.458	16	1.371803	1.14E-02	OL	7.30E+28	a	8.10E+28	a
C/1998 U5 (LINEAR)	19981221.7601	-31.428	-4.076	11	1.236452	1.01E-02	OL	4.75E+28	-2.1±0.2	a	a
C/1999 H1 (Lee)	19990711.1732	-66.544	69.933	50	0.708073	1.31E-03	YL	2.86E+29	-2.0±0.2	2.35E+29	-3.4±0.1
C/1999 N2 (Lynn)	19990723.0505	-44.041	65.450	44	0.761284	3.45E-03	OL	4.11E+28	-3.2±0.4	3.72E+28	-3.1±0.2
C/1999 J3 (LINEAR)	19990920.1662	-36.386	61.730	28	0.976811	1.15E-03	YL	3.26E+28	-4.1±0.5	3.56E+28	-0.13±0.3
C/1999 S4 (LINEAR)	20000726.1685	-66.239	19.448	48	0.765007	3.21E-06	DN	3.22E+28	-1.2±0.2	4.02E+25	-19.6±5.2
C/1999 T1 McNaught-Hartley	20001213.4205	-40.428	62.792	52	1.173711	1.15E-03	YL	5.76E+29	-2.4±0.7	5.28E+29	-3.3±0.2
C/2001 A2 (LINEAR)	20010524.5240	-61.000	64.906	67	0.778609	1.07E-03	YL	7.35E+28	-5.3±0.4	1.44E+29	-3.7±0.1
C/2000 WM1 (LINEAR)	20020122.6773	-51.696	46.379	60	0.555310	5.32E-04	YL	1.08E+29	-1.6±0.1	2.36E+29	-1.1±0.2
C/2001 OG108 (LONEOS)	20020315.0978	-42.445	28.197	11	0.994847	7.65E-02	OL	2.35E+28	a	6.75E+27	a
C/2002 C1 IP153) Ikeya-Zhang	20020318.9828	-44.542	120.498	63	0.507934	1.97E-02	OL	1.58E+29	-2.9±0.2	2.63E+29	-2.6±0.1
C/2002 G3 (SOHO)	20020416.7000	-40.270	-9.068	15	0.079400	1.02E-03	YL	2.18E+29	a	b	a
C/2002 O4 (Hoenig)	20021001.9400	-72.876	17.858	28	0.775735	-7.64E-04	DN	1.58E+28	a	5.30E+29	a
C/2002 X5 (Kudo-Fujikawa)	20030128.9761	-41.691	50.615	34	0.190286	1.07E-03	YL	9.19E+28	-2.1±0.2	5.53E+28	-1.8±0.2
C/2002 V1 (NEAT)	20030218.2881	-47.029	65.061	38	0.099256	2.29E-03	OL	8.62E+28	-2.6±0.1	1.78E+29	-1.5±0.2
C/2002 Y1 (Juels-Holvorcem)	20030413.2491	-88.291	94.668	62	0.713667	4.11E-03	OL	9.57E+28	-3.6±0.1	1.95E+29	-2.4±0.1
C/2002 T7 (LINEAR)	20040423.0763	-141.379	105.474	68	0.614585	2.89E-05	DN	1.10E+30	-1.8±0.1	3.55E+29	-2.1±0.1
C/2001 Q4 (NEAT)	20040515.9546	-212.872	170.986	147	0.961886	6.04E-05	YL	7.62E+29	-2.1±0.1	3.02E+29	-1.7±0.1
C/2003 K4 (LINEAR)	20041013.7066	-126.527	125.092	72	1.023580	2.79E-05	DN	4.83E+29	-1.7±0.2	5.62E+29	-1.7±0.1
C/2004 Q2 (Machholz)	20050124.9190	-143.724	119.311	78	1.205709	4.06E-04	YL	5.91E+29	-2.0±0.1	6.49E+29	-3.7±0.1
C/2006 M4 (SWAN)	20060928.7285	-79.025	89.000	51	0.783008	2.05E-04	YL	1.50E+29	-2.7±0.2	2.35E+29	-2.9±0.2
C/2006 P1 (McNaught)	20070112.7991	-35.886	77.439	60	0.170752	2.98E-05	DN	7.40E+29	-2.1±0.1	5.20E+29	-2.5±0.1
C/2007 F1 (LONEOS)	20071028.7593	-43.520	34.790	47	0.402402	-1.70E-04	DN	6.11E+28	-1.0±0.1	8.19E+27	-3.9±0.1
C/2007 N3 (Lulin)	20090110.6117	0.261	101.321	63	1.211769	3.12E-05	DN	b	b	1.78E+29	-1.7±0.1
C/2009 K5 (McNaught)	20100430.0228	-13.775	27.522	32	1.422394	4.94E-05	DN	b	b	1.46E+29	-0.7±0.5
C/2009 R1 (McNaught)	20100702.6852	-56.764	47.193	64	0.405037	-4.51E-05	DN	1.28E+29	-1.9±0.1	6.63E+28	-2.7±0.1
C/2009 P1 (Garradd)	20111223.6776	-129.718	105.384	117	1.550537	4.20E-04	YL	2.76E+29	-0.5±0.2	6.77E+29	-3.2±0.2

	T-Perihelion	T-Begin	T-End	N	q(AU)	a₀(AU)	Class	Q1-pre	p-pre	Q1-post	p-post
C/2012 E2 (SWAN)	20120315.0351	-12.084	-6.112	5	0.007164	2.36E-04	YL	5.11E+26	-3.3±0.4	b	b
C/2011 L4 (PanSTARRS)	20130310.1699	-44.470	51.389	50	0.301545	2.96E-05	DN	1.30E+29	-1.3±0.1	5.00E+28	-2.3±0.3
C/2012 F6 (Lemmon)	20130324.5151	-105.443	99.409	109	0.731248	2.19E-03	OL	3.20E+29	-3.0±0.1	4.80E+29	-2.3±0.1
C/2012 S1 (ISON)	20131128.7792	-34.901	-5.148	22	0.012444	-7.57E-05	DN	1.08E+29	-3.0±0.1	b	b
C/2013 R1 (Lovejoy)	20131222.7339	-69.730	91.039	141	0.811819	2.75E-03	OL	7.61E+28	-2.2±0.1	9.09E+28	-1.6±0.1
C/2012 K1 (PanSTARRS)	20140827.6559	-126.088	102.044	138	1.054531	2.46E-05	DN	2.00E+29	-0.8±0.2	1.90E+29	-2.4±0.3
C/2013 V5 (Oukaimeden)	20140928.2249	-38.435	10.633	41	0.625506	8.36E-06	DN	3.40E+28	-1.0±0.1	7.0E+28	-0.2±0.02
C/2014 Q2 (Lovejoy)	20150130.0781	-61.833	122.456	138	1.290484	1.99E-03	YL	2.30E+30	-6.6±0.6	1.90E+30	-3.4±0.1
C/2014 Q1 (PanSTARRS)	20150706.5128	-46.609	34.885	31	0.314557	1.20E-03	YL	5.30E+27	-7.8±0.1	9.10E+26	-8.9±0.1
C/2013 US10 (Catalina)	20151115.7201	-137.27	97.077	119	0.822956	5.97E-05	DN	2.80E+29	-1.6±0.1	1.60E+29	-1.9±0.1
C/2014 E2 (Jacques)	20140702.5164	-88.844	110.226	97	0.663946	1.25E-03	OL	1.50E+29	-2.4±0.2	1.10E+29	-1.7±0.1
C/2015 G2 (MASTER)	20150523.8022	-45.896	34.098	59	0.779772	5.45E-05	YL	4.10E+28	-1.8±0.2	6.65E28	-0.7±0.3
C/2013 X1 (PanSTARRS)	20160420.7226	-127.769	102.222	121	1.314254	2.41E-04	YL	8.20E+29	-3.0±0.1	2.70E+29	-2.2±0.1

Notes to Table 1
T-Perihelion - Date of perihelion yyyymmdd.frac
T-Begin - Start time image in days from perihelion
T-End - End time image in days from perihelion
N - number of images
q(AU) - perihelion distance in AU
a_0 (AU) - original semi-major axis
Class - DN (dynamically new), YL (young long period), OL (old long period), following A'Hearn et al. (1995), see text for definition
Q1-pre - production rate at 1 AU from power law fitted to pre-perihelion observations
p-pre - power-law exponent fitted to pre-perihelion observations
Q1-post - production rate at 1 AU from power law fitted to post-perihelion observations
p-post - power-law exponent fitted to post-perihelion observations
a. A power law did not represent the variation of Q with r.
b. No or too little data available.

Table II. Observational and Orbital Aspects of Short Period Comets Observed by SOHO SWAN

Comet	T-Perihelion	T-Begin	T-End	N	q	e	i	a	T$_J$
2P/Encke (1997)	19970523.5987	-3.179	34.408	15	0.331396	0.850014	11.9294	2.209513	3.026452
2P/Encke (2000)	20000909.6611	-38.75	34.765	18	0.339537	0.846898	11.7557	2.217718	3.025800
2P/Encke (2003)	20031229.8768	-28.244	-2.477	14	0.338461	0.847339	11.7696	2.217076	3.025448
2P/Encke (2007)	20070419.3117	-30.174	53.836	38	0.339269	0.847040	11.7543	2.218024	3.025237
2P/Encke (2010)	20100806.5019	7.242	38.163	7	0.335869	0.848338	11.7831	2.214589	3.025628
2P/Encke (2013)	20131121.6945	-45.701	-4.063	38	0.336127	0.848232	11.7790	2.214742	3.025716
2P/Encke (2017)	20170310.0924	-42.109	40.938	57	0.335895	0.848334	11.7782	2.214702	3.025546
8P/Tuttle (2008)	20080127.0256	-18.759	21.493	33	1.027117	0.819800	54.9832	5.699872	1.600663
9P/Tempel 1 (2005)	20050705.3153	-0.577	24.875	9	1.506167	0.517491	10.5301	3.121531	2.970018
17P/Holmes (2007)	20070419.3117	174.338	199.001	23	0.339269	0.847040	19.1132	2.218024	3.001528
19P/Borrelly (2001)	20010914.7055	-72.586	106.195	76	1.358096	0.623798	30.3238	3.610018	2.565162
21P/Giacobini-Zinner (1998)	19981121.3205	-1.208	28.218	18	1.033713	0.706483	31.8588	3.521816	2.466428
21P/Giacobini-Zinner (2005)	20050702.7605	-54.877	26.31	39	1.037914	0.705691	31.8109	3.526613	2.466711
21P/Giacobini-Zinner (2012)	20120211.7347	45.490	27.158	37	1.030489	0.707045	31.9106	3.517568	2.466276
24P/Schaumasse (2001)	20010502.6917	9.592	34.828	4	1.205203	0.704923	11.7505	4.084368	2.504373
41P/Tuttle-Giacobini-Kresak (2001)	20010106.9664	-47.354	23.318	34	1.052233	0.659237	9.2255	3.087873	2.828496
41P/Tuttle-Giacobini-Kresak (2006)	20060611.7914	-40.537	31.679	27	1.047777	0.660413	9.2280	3.085445	2.827795
41P/Tuttle-Giacobini-Kresak (2017)	20170412.7519	-12.081	8.623	13	1.045044	0.661243	9.2293	3.084937	2.826863
45P/Honda-Mrkos-Pajdusakova (2001)	20010329.9268	-2.952	50.023	21	0.528411	0.825078	4.2556	3.020838	2.581000
45P/Honda-Mrkos-Pajdusakova (2011)	20110928.7813	-33.093	46.142	46	0.529641	0.824626	4.25233	3.020066	2.582336
45P/Honda-Mrkos-Pajdusakova (2017)	20161231.2670	-15.322	47.465	26	0.532555	0.823995	4.24940	3.025795	2.581290
46P/Wirtanen (1997)	19970314.1501	-50.819	47.957	44	1.063764	0.656748	11.7225	3.099076	2.818571
46P/Wirtanen (2002)	20020826.6791	-43.643	64.142	28	1.058618	0.657747	11.7381	3.093086	2.819340
55P/Tempel-Tuttle (1998)	19980228.0975	-56.783	59.802	36	0.976576	0.905518	162.4862	10.336106	0.637301
67P/Churyumov-Gerasimenko (1996)	19960117.6564	5.173	34.15	4	1.300034	0.630192	7.1133	3.515430	2.746628
67P/Churyumov-Gerasimenko (2002)	20020818.2877	-2.723	27.736	10	1.290650	0.631750	7.1240	3.504820	2.747102
67P/Churyumov-Gerasimenko (2009)	20090228.2985	2.231	50.378	28	1.247284	0.640337	7.0418	3.467924	2.744986
73P/Schwassmann-Wachmann 3 (2001)	20010127.7149	-24.731	80.026	52	0.937355	0.693815	11.4061	3.061401	2.782496
73P/Schwassmann-Wachmann 3-B (2006)	20060607.9244	-65.189	-9.886	24	0.939111	0.693286	11.3970	3.061846	2.783129
73P/Schwassmann-Wachmann 3-C (2006)	20060606.9570	-66.264	53.485	52	0.939146	0.693207	11.3958	3.061172	2.783503

	T-Perihelion	T-Begin	T-End	N	q(AU)	e	i	a	T_J
81P/Wild 2 (1997)	19970506.6272	-37.071	53.649	33	1.582622	0.540221	3.2426	3.442136	2.878274
96P/Machholz 1 (1996)	19961015.0696	-15.728	26.043	8	0.124718	0.958637	60.0742	3.015207	1.941717
96P/Machholz 1 (2002)	20020108.6268	-14.317	25.249	12	0.124110	0.958243	60.1857	2.972196	1.965408
96P/Machholz 1 (2007)	20070404.6194	-23.725	25.39	24	0.124618	0.958684	59.9553	3.016216	1.941834
96P/Machholz 1 (2012)	20120714.7852	10.194	20.198	4	0.123791	0.959182	58.2989	3.032755	1.942448
103P/Hartley 2 (1997)	19971222.0173	-50.518	97.534	50	1.031722	0.700375	13.6189	3.443378	2.639661
103P/Hartley 2 (2010)	20101028.2570	-42.853	45.608	61	1.058690	0.695145	13.6169	3.472766	2.639781
141P/Machholz 2 (1999)	19991209.9566	-41.387	47.507	13	0.748991	0.751078	12.8119	3.008939	2.708274

Notes for Table 2
T-Perihelion = Time /Date of perihelion yyyymmdd.fraction
T-Begin = first image in days from perihelion
T-End = last image in days from perihelion
N = number of images
q(AU) = perihelion distance in AU
e = eccentricity of orbit
i = inclination of orbit in degrees
a = semi-major axis of orbit in AU
T_J = Tisserand constant with Jupiter

Table 3. Observational Results of Individual Apparitions of Short Period Comets Observed with SOHO SWAN

Comet	r_N	Q-1AU	p-pre	Q-1AU	p-post	AApre	AApost	AFpre	AFpost
2P/Encke (1997)	2.40	b	b	2.13E+28	-1.0±0.3	-	1.34	-	0.0185
2P/Encke (2000)	2.40	8.18E+27	-3.1±0.7	1.01E+28	-3.2±0.5	0.51	0.63	0.0071	0.0088
2P/Encke (2003)	2.40	9.98E+27	-1.0±0.2	b	b	0.63	-	0.0086	-
2P/Encke (2007)	2.40	1.60E+28	-0.7±0.3	9.12E+27	-2.0±0.2	1.00	0.57	0.0139	0.0079
2P/Encke (2010)	2.40	b	b	5.11E+27	-2.4±0.5		0.32		0.0044
2P/Encke (2013)	2.40	4.58E+28	-2.4±0.1	b	b	2.87		0.0397	
2P/Encke (2017)	2.40	7.93E+27	-1.1±0.2	9.23E+27	-2.1±0.2	0.50	0.58	0.0069	0.0080
8P/Tuttle (2008)	2.25	4.11E28	-8.9±0.1	3.42E28	3.2±0.1	2.58	2.15	0.0405	0.0337
9P/Tempel 1 (2005)	2.72	a	a	a	a	-	-	-	-
17P/Holmes (2007)	1.61	a	a	b	b	-	-	-	-
19P/Borrelly (2001)	2.40	2.80E+29	-5.2±1.1	3.50E+29	-6.6±0.6	17.56	21.95	0.2426	0.3032
21P/Giacobini-Zinner (1998)	1.82	b	b	4.04E+28	-9.0±0.9	-	2.53	-	0.0609
21P/Giacobini-Zinner (2005)	1.82	5.88E+29	-1.7±0.4	8.10E+28	-18.5±3.5	36.87	5.08	0.8858	0.1220
21P/Giacobini-Zinner (2012)	1.82	2.30E+29	-11.9±0.2	2.44E+29	-11.1±0.1	14.42	15.3	0.3465	0.3268
24P/Schaumasse (2001)	b	b	b	b	b	-	-	-	-
41P/Tuttle-Giacobini-Kresak (2001)	0.70	2.53E+28	--5.9±0.1	7.09E+29	-7.9±0.5	1.59	44.46	0.2578	7.220
41P/Tuttle-Giacobini-Kresak (2006)	0.70	1.89E+28	-2.6±0.5	2.15E+28	a	1.19	1.35	0.1925	0.2190
41P/Tuttle-Giacobini-Kresak (2017)	0.70	1.59E+27	a	4.07E+27	a	0.10	0.26	0.0162	0.0413
45P/Honda-Mrkos-Pajdusakova (2001)	0.39	b	b	6.52E+27	-3.6±0.4	-	0.41	-	0.2139
45P/Honda-Mrkos-Pajdusakova (2011)	0.39	6.47E+26	-6.6±0.1	1.46E+28	-2.8±0.1	0.04	0.92	0.0212	0.4790
45P/Honda-Mrkos-Pajdusakova (2017)	0.39	2.24E+27	-4.2±0.2	1.27E+28	-2.0±0.1	0.14	0.80	0.0735	0.4167
46P/Wirtanen (1997)	0.6	1.78E+28	-3.6±0.1	1.84E+28	-0.9±0.1	1.12	1.15	0.0617	0.0637
46P/Wirtanen (2002)	0.6	2.13E+28	a	4.24E+28	-3.9±1.4	1.34	2.66	0.0738	0.1469
55P/Tempel-Tuttle (1998)	1.80	4.95E+28	-6.3±0.4	4.13E+28	-1.7±0.3	3.10	2.59	0.0762	0.0636
67P/Churyumov-Gerasimenko (1996)	2.00	b	b	4.43E+28	-4.5±2.3	-	2.78	-	0.0553
67P/Churyumov-Gerasimenko (2002)	2.00	b	b	a	-12±11	-	-	-	-
67P/Churyumov-Gerasimenko (2009)	2.00	b	b	2.32E+28	-4.3±2.1	-	1.46	-	0.0289
73P/Schwassmann-Wachmann 3 (2001)	1.26	7.40E+28	-0.8±3.0	8.44E+28	-2.1±0.3	4.64	5.29	0.2326	0.2653
73P/Schwassmann-Wachmann 3-B (2006)	b	1.75E+28	-1.3±1.0	b	b	1.10	-	-	-
73P/Schwassmann-Wachmann 3-C (2006)	b	1.97E+28	-2.2±0.4	1.23E+28	-6.9±0.9	1.24	0.77	-	-

Comet (year)	rN	Q1-pre	p-pre	Q1-post	p-post	AA pre	AA post	AF pre	AF post
81P/Wild 2 (1997)	2.10	a	a	a	a				
96P/Machholz 1 (1996)	3.20	7.12E+26	-3.5±0.1	6.84E+27	-2.4±1.2	0.045	0.429	0.00035	0.0033
96P/Machholz 1 (2002)	3.20	1.74E+27	-2.4±0.3	1.46E+28	-0.8±0.8	0.109	0.916	0.00085	0.0071
96P/Machholz 1 (2007)	3.20	2.54E+27	-2.9±0.5	5.04E+27	-2.3±0.2	0.159	0.316	0.00124	0.0025
96P/Machholz 1 (2012)	3.20	b	b	4.33E+27	-2.9±0.4	-	0.272	-	0.0021
103P/Hartley 2 (1997)	0.54	3.94E+28	-6.6±0.1	3.08E+28	-3.2±0.1	2.47	1.931	0.6743	0.5271
103P/Hartley 2 (2010)	0.54	2.31E+28	-14.0±1.0	1.35E+28	-7.2±1.2	1.45	0.847	0.3953	0.2310
141P/Machholz 2 (1999)	b	7.45E+27	-0.4±0.9	1.79E+27	-5.3±1.1	0.47	0.139	-	-

Notes for Table 3

r_N = nucleus radius in km.

Q1- pre = power law water production rate in molecules s^{-1} at 1 AU for pre-perihelion observations

p-pre = power law exponent for pre-perihelion observations

Q1- post = power law water production rate in molecules s^{-1} at 1 AU for post-perihelion observations

p-post = power law exponent for post-perihelion observations

AA pre = active area in km^2 at 1 AU for pre-perihelion observations

AA post = active area in km^2 at 1 AU for post-perihelion observations

AF pre = active fraction at 1 AU for pre-perihelion observations

AF post = active fraction at 1 AU for post-perihelion observations

a. A power law did not represent the variation of Q with r.

b. No or too little data available.

References for nucleus radii r_N in km

2P/Encke - 2.4±0.3 Fernandez et al. (2000)

8P/Tuttle - 2.25±0.5 Equivalent single sphere from Harmon et al. (2008); Harmon et al. (2010) radar observation

9P/Tempel 1 - Lamy et al. (2007) verified by s/c flyby

17P/Holmes - Snodgrass, Lowry and Fitzsimmons (2006)

19P/Borrelly - 2.40 Weaver et al. (2003), verified by s/c flyby

21P/Giacobini-Zinner - Pittichova et al. (2008)

41P/ Tuttle-Giacobini-Kresak - Lamy et al (2004); Howell et al. (2017) r>0.45 km radar

46P/Wirtanen -- Lamy et al (2004) gives individual values of 0.62 0.56, 0.7, 0.6

45P/HMP - Fernandez, J. (private communication); Lowry et al. (2003) 1.34km; Tancredi et al. 0.33 km;

67P/Churyumov-Gerasimenko -- Lamy et al. (2007), mean spherical radius agrees with Rosetta images.

46P/Wirtanen - Lamy et al. (1998)

55P/Tempel-Tuttle - Lamy et al. (2004) Comets II

73P/SW3 in 2001 - Boehnhardt et al. (1999)

81P/Wild 2 - Fernandez et al. (2013)

96P/Machholz 2 - Schleicher (2008); Lamy et al. (2004) quotes values of (3.5, 2.8 and 3.2) that gives 3.2 ±0.2

103P/Hartley 2 - Lisse et al. (2006) verified by s/c flyby

Table 4. Average Results for Multiple-Apparitions of Short Period Comets Observed with SOHO SWAN

Comet	r_N	Q1-pre	p-pre	Q1-post	p-post	AApre	AApost	AFpre	AFpost
2P/Encke (1997, 2000, 2003, 2007, 2010, 2013, 2017)	2.40	6.59E+27	-1.8±0.1	1.04E+28	-2.1±0.2	0.58	0.65	0.0080	0.0090
21P/Giacobini-Zinner (1998, 2005, 2012)	1.82	4.79E+28	-1.2±0.8	4.54E+28	-11.7±1.6	3.00	2.85	0.0722	0.0684
45P/Honda-Mrkos-Pajdusakova (2000, 2011, 2017)	0.39	8.55E+26	-5.9±0.3	6.26E+27	-3.7±0.2	0.05	0.39	0.0281	0.2054
46P/Wirtanen (1997, 2002)	0.6	1.68E+28	-3.6±0.7	2.89E+28	-3.4±1.3	1.82	1.09	0.4615	0.2769
96P/Machholz (1996, 2002, 2007, 2012)	3.20	2.52E+27	-2.5±0.7	6.77E+27	-1.9±0.2	0.16	0.42	0.0012	0.0033

Notes for Table 4
Comet name with perihelion year of apparitions included in the averages
rN = nucleus radius in km.
Q1- pre = power law water production rate in molecules s^{-1} at 1 AU for pre-perihelion observations
p-pre = power law exponent for pre-perihelion observations
Q1- post = power law water production rate in molecules s^{-1} at 1 AU for post-perihelion observations
p-post = power law exponent for post-perihelion observations
AA pre = active area in km^2 at 1 AU for pre-perihelion observations
AA post = active area in km^2 at 1 AU for post-perihelion observations
AF pre = active fraction at 1 AU for pre-perihelion observations
AF post = active fraction at 1 AU for post-perihelion observations

Table 5. Taxonomic Classes of SWAN Comets

Typical Short Period: 2P/Encke, 8P/Tuttle, 9P/Tempel 1, 45P/Honda-Mrkos-Pajdusakova, 46P/Wirtanen, 55P/Tempel-Tuttle, 67P/Churyumov-Gerasimenko, 103P/Hartley 2, 153P/ Ikeya-Zhang, 141P/Machholz 2

Depleted Short Period: 19P/Borrelly, 21P/Giacobini-Zinner, 81P/Wild 2, 96P/Machholz 1

Typical Long Period: C/1996 B2 (Hyakutake), C/1995 O1 (Hale-Bopp), C/1999 H1 (Lee), C/2001 A2 (LINEAR), C/2000 WM1 (LINEAR), C/2004 Q2 (Machholz), C/2007 N3 (Lulin), C/2009 R1 (McNaught), C/2012 F6 (Lemmon), C/2012 S1 (ISON), C/2014 Q2 (Lovejoy)

Depleted Long Period: C/1999 S4 (LINEAR), C/2012 K1 (PanSTARRS), C/2013 R1 (Lovejoy)

Table 6. Comparison of Water Production Power-law Exponents with Taxonomic Class

Comet	Number of Comets	Power-Law Exponent
Typical Short Period	4	-3.25
Depleted Short Period	3	-4.33
Typical Long Period	11	-2.62
Depleted Long Period	3	-1.82